Spectral extrapolation principles and application: Mindoro Island, Philippines, seismic data

Charles Ian Puryear[1], Raghava Tharimela[2], Dhirendra Ray[3], Vsevolod Egorov[1], Graeme Baille[4], and Agus Imran Hernandianto[5]

Abstract

Spectral extrapolation is a bandwidth extension technique that we implement by combining spectral inversion with constraints, time-variant wavelet extraction, and targeted broadband filtering. We explain the principles of spectral extrapolation as a valid and effective bandwidth extension method and demonstrate its application to a 2D onshore Philippines legacy seismic data set using a time-variant wavelet extraction, resulting in a tripling of the frequency range of the spectrum. The results indicate significant potential for mapping complex stratigraphy and geomorphological features not evident on the input seismic data images, yielding information about reservoir distribution and connectivity that is often critical for optimal well placement.

Introduction

Bandwidth extension (BE) has a long history of successful application in electrical engineering applications, including audio and speech enhancement. Due to its potential for enhancing the quality of seismic data at low cost, BE has received increasing attention and has been a common subject of research and development in recent decades. While the objective is clear — to increase the resolution of seismic data in order to provide the interpreter with a better view of stratigraphic and structural details — optimal implementation is not straightforward.

To address resolution issues in processing, Canadas (2002) defined regularization conditions for blind sparse seismic deconvolution. Spectral inversion as a means of increasing seismic resolution was introduced by Partyka (2005) and Portniaguine and Castagna (2005).

Our spectral extrapolation (SE) implementation is a technique for BE that combines spectral inversion with a time-variant wavelet and targeted broadband filtering. This implementation builds on the work done by Puryear and Castagna (2008), which described an inversion formulation that decomposes seismic data using a basis of even and odd dipole layer responses in the frequency domain. The technique has been applied to prestack data (Rubino and Velis, 2009). The implementation described in this work assumes that band-limited seismic data are constructed by nonstationary convolution of the seismic reflectivity with a time-variant band-limited wavelet, i.e., time-variant wavelet convolution as outlined by Margrave (1998). In our approach, the time-variant wavelet is estimated. The bandwidth of the seismic data is then extended by multiplying the estimated dipole layer responses with a broadband filter in the frequency domain (equivalent to convolution in the time domain).

Zhang and Castagna (2011) implement sparse layer inversion in the time domain; spectral inversion is implemented in the frequency domain. Advantages of frequency-domain inversion include the following: (1) the inversion model space is limited to the wavelet band frequency range with an acceptable signal-to-noise ratio, thereby acting as a natural noise filter and reducing computational cost; and (2) constraints on the shape of the spectrum (such as matching the input spectrum or shaping) can be readily applied.

The dipole layer decomposition is generally applicable to seismic data in which geologic layering tends to generate reflection coefficients in closely spaced pairs, but it tends to fail where reflections are chaotic (i.e., salt, debris flows, or reefs). In applicable cases, BE is valid, and the method effectively uncovers stratigraphic architecture that is masked by the low-frequency wavelet operator in the input seismic data.

Effective BE also relies on appropriate input seismic data. To obtain optimal results, we rotate the seismic data to zero phase and condition with appropriate denoising such as band-pass and structural filtering.

The result can be used as a broadband alternative input to conventional workflows such as seismic inversion (Leiceaga and Puryear, 2019) and machine learning 3D rock properties prediction (Puryear et al., 2021). In this work, we review the principles of SE and present an example of their application to 2D seismic data collected onshore Mindoro Island, Philippines.

Methodology

One common definition of bandwidth is the range of frequencies in the spectrum:

$$B_w = \xi_h - \xi_l, \tag{1}$$

where ξ_l and ξ_h are the minimum and maximum frequencies (Hz) of the spectrum, respectively. Seismic resolution has a complicated nonlinear relationship to bandwidth and frequency. For seismic frequencies (at the relatively low end of the acoustic spectrum) and assuming a flat or symmetrical spectrum, we can approximate the two-way traveltime tuning thickness (s) as an inverse function of bandwidth:

$$b = 1 / B_w, \tag{2}$$

[1]Spectral Geosolutions, Houston, Texas, USA. E-mail: charles@spectralgeosolutions.com; seva@geoexpera.com.
[2]Spectral Geosolutions, Hyderabad, Telangana, India. E-mail: raghava.tharimela@spectralgeosolutions.com.
[3]Ray Speed Solutions Pvt. Ltd., Gurugram, Haryana, India. E-mail: dhirendra.ray@rayspeedsolutions.com.
[4]Spectral Geosolutions, Brisbane, Queensland, Australia. E-mail: gbaille@spectralgeosolutions.com.
[5]Spectral Geosolutions, Cilandak, South Jakarta, Indonesia. E-mail: agus.hernandianto@spectralgeosolutions.com.

where B_w is the bandwidth and b is the tuning thickness. Thus, resolution is directly proportional to bandwidth, assuming the frequency content is accurate and other factors such as noise and reflectivity contrast have a consistent effect across the spectrum. Note that this formulation is merely a heuristic and not a processing requirement.

BE of a signal can be defined as "the deliberate process of expanding the frequency range (bandwidth) of a signal in which it contains an appreciable and useful content, and/or the frequency range in which its effects are such" (Aarts et al., 2003). Therefore, if a process introduces appreciable frequency content outside of the input band that is *useful*, then it is a BE process. For seismic BE, we utilize the following criteria to evaluate the result: (1) agreement with layering observed in well logs and (2) geologically realistic character. The question is: does SE fulfill these criteria?

Figure 1 illustrates the concept of SE. The input spectrum (blue) with usable signal is approximately 5–45 Hz. Through
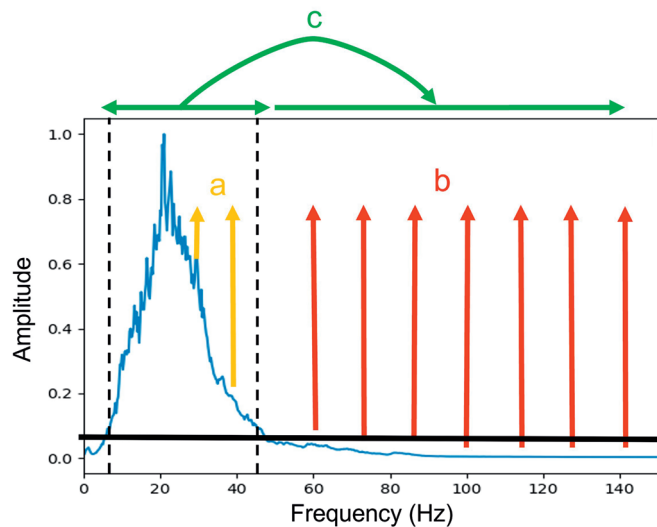

Figure 1. Typical seismic spectrum with illustration of several frequency enhancement methods: (a) valid spectral whitening boosts the high frequencies within the wavelet band; (b) overapplication of inverse filter boosts noise at high frequencies; and (c) SE uses information within the seismic band to extrapolate to higher frequencies.
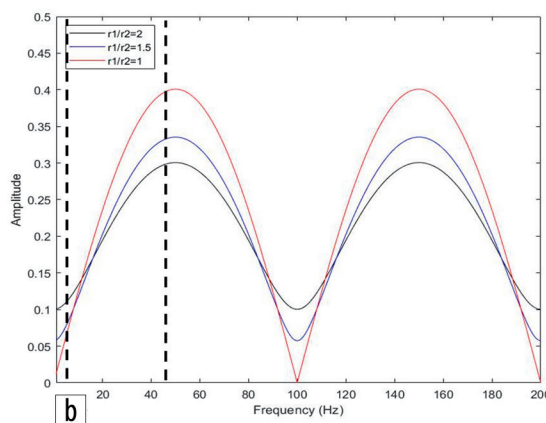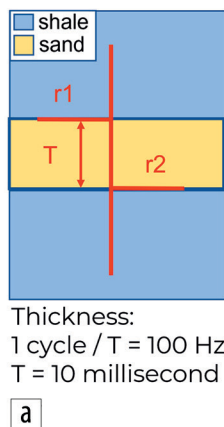
application of spectral whitening, the high end of the spectrum can be enhanced by simply boosting the high-frequency components of the wavelet spectrum as indicated by the orange arrows. This method is valid and can yield moderate enhancements in resolution and visualization of thin layers. However, the process is often taken too far. An inverse filter, as shown by the red arrows, when applied outside the wavelet band, boosts noise and results in degradation of the image. In SE, we use the frequency content from the input wavelet band to reliably predict information in the high-frequency (noise) space (green arrows). The bulk statistical autocorrelation wavelet within the analysis window provides an estimate of these band limits. Both signal and noise will be extrapolated to some extent, but the noise can be effectively suppressed by application of structural filtering before and/or after the SE process.

Figure 2 shows the amplitude spectrum for an odd dipole (same magnitude/opposite polarity) reflection coefficient pair in the time and frequency domains. The reflectivity is modeled as a typical thin low-impedance sand encased in shale. This manifests in the frequency domain as a sinusoidal function with a period inverse to the layer thickness. The reflection coefficient ratio is varied, but, importantly, the periodicity of the response remains constant (i.e., it is controlled by thickness and not the reflection coefficient ratio), indicating a deterministic connection between the wavelet band and adjacent frequency bands. For illustration, the wavelet band is assumed to be the same as in Figure 1 (5–45 Hz). The objective of SE is to accurately extend the harmonic (periodic) patterns within the wavelet band to the noise space of the spectrum.

Some questions that commonly arise on the topic of SE and resampling are:

- *Does SE require resampling?* Generally, the answer is yes, but it depends on two factors: (1) the Nyquist/antialiasing cutoff frequency of the data and (2) the high-cut limit for SE.
- *Is it possible to define frequencies beyond the Nyquist or antialiasing filter cutoff frequency?* By resampling, we create an extended frequency space as well as the potential for estimation of frequency information well beyond the original Nyquist or antialiasing filter cutoff frequency.

In general, SE requires a two-stage process: (1) upsampling to a finer sampling rate, which can be accomplished by fast Fourier transform zero padding or sinc interpolation, and (2) extrapolation or projection of the information within the wavelet band into the frequency space created by resampling the data. Figure 3 illustrates upsampling in (a) the time domain and (b) the frequency domain. In the time domain, the trace data are resampled from a typical seismic sampling rate of dt = 4 ms to dt_{resamp} = 1 ms; this correspondingly increases the capacity of the data in the

Figure 2. (a) Model of low-impedance thin sand encased in shale and (b) amplitude spectrum with varying reflection coefficient ratios. The shaded region indicates the same wavelet band shown in Figure 1.

frequency domain (i.e., creates a suitable "container" for the SE output). For dt = 4 ms, the Nyquist frequency is

$$\xi_{Nyquist} = 1 / (2dt) = 125 \text{ Hz.} \qquad (3)$$

However, a conservative antialiasing filter of approximately 75% of Nyquist is often applied to the data. Thus, in this case, the maximum usable frequency is 93.75 Hz:

$$\xi_{max} = .75\xi_{Nyquist} = 93.75 \text{ Hz.} \qquad (4)$$

With this antialiasing factor, no process (including SE) can generate reliable frequency content beyond this limit for data sampled at 4 ms. However, if we simply resample the data to 1 ms, then the maximum potential frequency is increased to 375 Hz:

$$\xi_{Nyquist} = 1 / (2dt) = 500 \text{ Hz, and} \qquad (5)$$

$$\xi_{max} = .75\xi_{Nyquist} = 375 \text{ Hz.} \qquad (6)$$

Note that, by resampling, we have merely increased the frequency *capacity* of the data; this modification does not guarantee that a BE process performed subsequently will recover accurate high-frequency information.

Wavelet convolution in the time domain is equivalent to multiplication in the frequency domain. In one approach to SE, a band-limited dipole basis matrix $B(\xi)$ is generated by element-wise multiplication of the complex wavelet spectrum $W(\xi)$ with the complex broadband dipole basis matrix $A(\xi)$ in the frequency domain, where ξ denotes ordinary frequency:

$$B(\xi) = W(\xi) * A(\xi). \qquad (7)$$

Next, we satisfy the following function:

$$\text{minimize } \left\| B(\xi)x - y(\xi) \right\|_2^2 + \alpha \|x\|_1, \xi_l < \xi < \xi_h. \qquad (8)$$

This is an ℓ_1-regularized least-squares program formulation of a basis pursuit denoising problem (Friedlander and Saunders, 2019), wherein $B(\xi)$ and $y(\xi)$ are the complex (frequency domain) band-limited basis matrix and data trace vector, respectively, x is the sparse layer coefficient solution vector, and α is a user-defined ℓ_1-regularization factor. The inverse problem is solved over the frequency range ξ_l to ξ_h, the minimum and maximum frequency limits of the wavelet band with an adequate signal-to-noise ratio. In practice, this range is generally determined by trial and error, along with α.

We further explore the concept of SE using a schematic of the process. Figure 4 illustrates a basis of time- and frequency-domain (imaginary) responses for odd dipole layers with variable thickness. For illustrative purposes, only three representative members of the basis are shown; the band-pass for a typical wavelet is indicated by the shaded region. In Figure 5, the response for a 10 ms layer is plotted in time and frequency space. Assuming a flat wavelet spectrum for simplicity, a model is created by band limiting the response and adding noise. The

solution, represented by sparse layer coefficients, is computed from a range of frequencies *within the wavelet band*. The quality of SE depends on accurately modeling the input data with $B(\xi)$, thereby resulting in a *useful* BE process. However, because the wavelet band-limited model $B(\xi)$ is simply a band-passed version of the broadband dipole response basis $A(\xi)$ (equation 7), the effective solution band far exceeds the wavelet band. Thus, frequencies outside of the wavelet band are recovered by utilizing a geologically suitable layering model and applying the sparse layer coefficient solution x (equation 8) to the dipole layer basis $A(\xi)$ with broadband filter (defined in workflow section). The
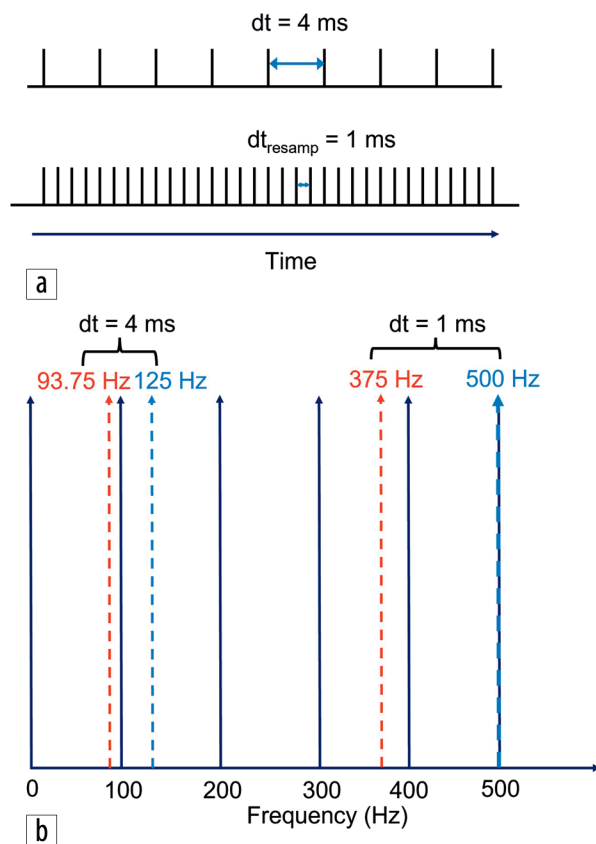

Figure 3. (a) Time domain resampling from dt = 4 ms to dt_{resamp} = 1 ms. (b) Nyquist frequencies 125 and 500 Hz (blue lines) and antialiasing frequencies 93.75 and 375 Hz (red lines) for the 4 ms and 1 ms sampling rates, respectively.
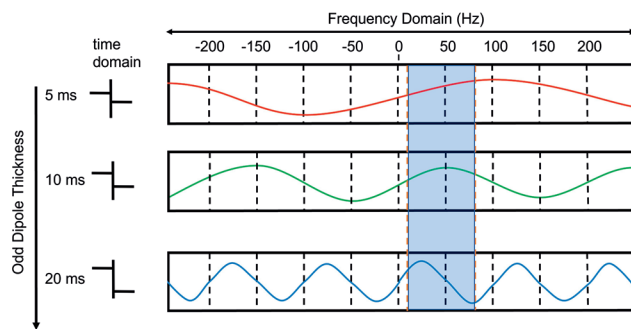

Figure 4. Schematic of a simplified frequency-domain basis of odd dipoles with varying thickness. The period is inverse to the time-domain thickness. The shaded region indicates the wavelet band limits for the dipole basis (inversion model).
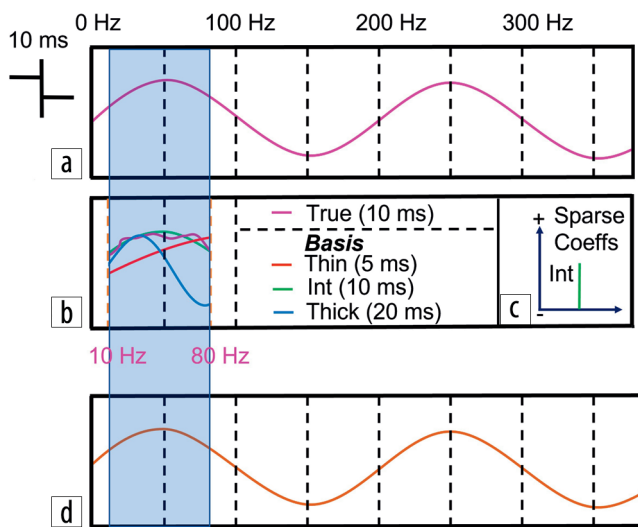
Special Section: Seismic resolution

Figure 5. (a) Time- and frequency-domain response for a 10 ms layer (shaded area represents wavelet band). (b) Band-passed model with flat wavelet spectrum and added noise together with the inversion basis. (c) Sparse layer coefficient solution (x in equation 8). (d) High-resolution solution (x applied to the original basis $A(\xi)$ without wavelet band-pass) recovering the true broadband input model response.
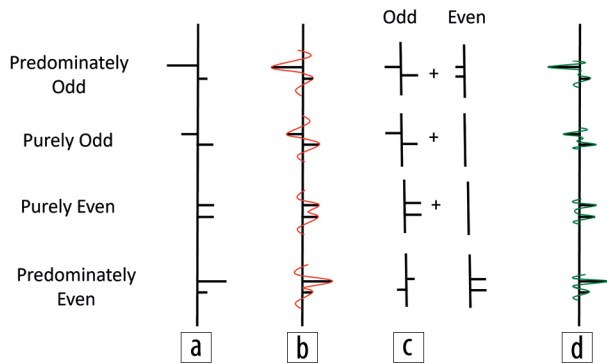

Figure 6. Illustration of the dipole decomposition process in the time domain: (a) the input model; (b) the input model convolved with the seismic wavelet (red); (c) even/odd decomposition; and (d) recomposed trace with frequency extended wavelet (green).
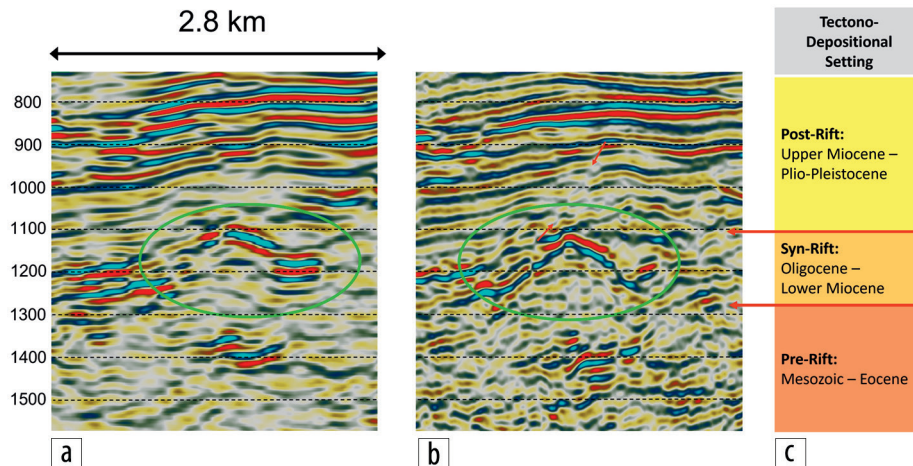

Figure 7. Comparison between the (a) the original seismic data and (b) reprocessed seismic data. Note the improvements in the quality of the image of the structural high (green circles) and associated reactivated fault propagating into the postrift section (marked by small red arrows). Continuity of the events on the reprocessed data is also increased. (c) Tectono-depositional setting column with sediment ages.

limits, in terms of output bandwidth, on our ability to effectively achieve this primarily depend on the input bandwidth, noise level, and accuracy of the extracted wavelet. Careful handling of phase, including constant amplitude/constant phase (CACP)-compliant processing (Lazaratos and Finn, 2004), also increases the overall accuracy of the process. The dipole decomposition process is illustrated in the time domain for different odd/even reflectivity configurations in Figure 6. The effect of wavelet extraction on SE is further explored in the results section, wherein a time-variant wavelet extraction approach is described.

Results

Philippines Mindoro data setting. We applied the SE method to a legacy onshore 2D seismic data set acquired on Mindoro Island, Philippines. This terrain rifted from the South China margin during the Early Oligocene, forming the easternmost segment of the Palawan-Mindoro microcontinent (Bird et al., 1993). On Mindoro Island, coarse clastics were derived from the uplifted collision zone. Unconformities separating stratigraphic sequences can be identified on seismic data with characteristic zones of stratigraphy and structure. The synrift sequence comprises terrigenous arkosic sandstones grading into marine deposits, including platform and reefal limestones. The regressive drift sequence grades from marine shales, sandstones, and detrital limestones to deltaic sands and shales. Reservoir and source rocks have been identified in this sequence. The legacy well used in this study allowed lithology and age determination of the penetrated sediments (Sarewitz and Karig, 1986). They consist of the prerift (Mesozoic to Eocene), rift (Oligocene-Lower Miocene), and postrift (Upper Miocene and younger) clastics and carbonates. The prerift sediments form a prominent structural high in the middle of the section.

Input data reprocessing. An important factor in generating useful SE results is the quality of the input. As is the case with any seismic processing sequence, a continuous chain of high-quality intermediate products leads to an optimal final product. In this case, prior to SE, the 2D seismic data were reprocessed to improve structural definition. The key steps in the processing sequence included noise attenuation, amplitude balancing, deconvolution, residual statics corrections, and common-depth-point domain interpolation to estimate missing traces. Next, a 2D Kirchhoff prestack time migration was run. The data are CACP compliant in that no whitening deconvolution, Q compensation, or deghosting was applied. The polarity is as follows: red is an increase in impedance. As shown in Figure 7, the structural high is better defined in the reprocessed data image, with improved layer continuity, thus leading to greater confidence in the SE results. Other differences in detectability, continuity, and geometry are also evident.

SE workflow overview. We applied the following workflow to implement SE:

1) window data to zones of interest 500–1600 ms and resample from dt = 2 ms to dt_{resamp} = 1 ms;
2) initial band-pass 0–8–60–90 Hz on the input data;
3) well-tie phase correction;
4) time-variant wavelet extraction and incorporation into the dipole inversion basis;
5) SE;
6) broadband filter 0–0–100–150 Hz on SE data; and
7) structural noise cancelation filter.

Workflow details. The initial band-pass eliminates noise outside the wavelet frequency band. For purposes of interpretation and further processing such as seismic inversion, it is desirable to correct the input data to zero phase. When available, well data can be used for this purpose by simply taking the seismic trace phase with maximum correlation to the synthetic generated using the zero-phase statistical wavelet. For these data, the max correlation phase value or zero-phase point was achieved by rotating the seismic phase by 13° (Figure 8). Note that this method does not account for the nonstationary (time-variant) phase. The well tie with phase correction for the original seismic data is shown in Figure 9.

While not a strict requirement for SE, it is generally advisable to use a time-variant wavelet when attenuation is expected to have a significant effect within the time window (i.e., in all but the shortest windows). This step yields a more accurate sparse reflectivity dipole solution and minimizes ringing artifacts. The wavelet is properly characterized as a *smoothly* varying operator dominated by attenuation with local perturbations created by reflectivity, rock and fluid effects. These short-period effects should be suppressed (not enhanced) by the time-variant wavelet extraction method. To this end, we extract a time-variant statistical wavelet using trace autocorrelation (Jones and Morrison, 1954; Cui and Margrave, 2014) with a 500 ms window and a window center step of 100 ms; the wavelet "nodes" are then interpolated in the time domain so that a smoothly varying wavelet is generated at each time sample (Figure 10). The most important limitation of this process is the assumption that the wavelet is zero phase. The Fourier transform $W(t,\xi)$ of the time-variant wavelet is incorporated into the basis matrix, which becomes $B(t,\xi)$ in equation 7.

The peak frequency of the data is approximately 20 Hz. The inversion basis comprises a range of thicknesses of even and odd dipoles (Puryear and Castagna, 2008) from 0 to 25 ms (the tuning thickness). This thickness set is then shifted along the trace sample by

sample and multiplied with the wavelet elementwise in the frequency domain to generate the complete basis. The 0 ms even component is a single spike that can account for layers thicker than the maximum. In lieu of explicit smoothing regularization across traces, which can strongly affect amplitudes, we apply a broadband filter and structural filtering, when warranted, to the SE result. The structural filter used in this example is a dip-guided median filter to reduce noise along reflectors (Brouwer and Huck, 2011).

The well tie for SE is shown in Figure 11. There is generally a trade-off between resolution and accuracy. In this example, a good match is achieved, but mismatches in the input are carried over or accentuated.

An important diagnostic for seismic data is the bulk statistical wavelet, which provides a visual synopsis of the data's frequency content/resolution. The extracted bulk statistical wavelets for the
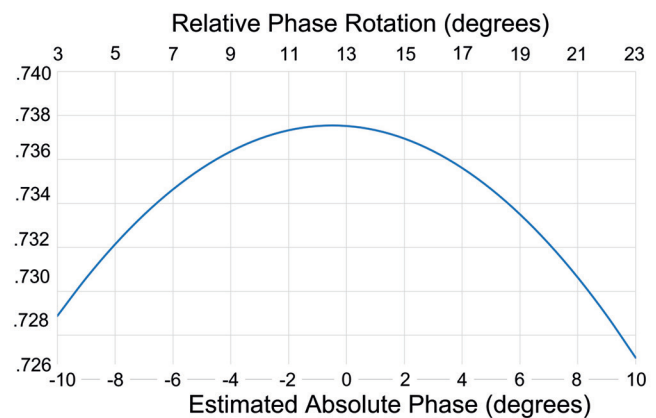

Figure 8. Phase rotation correlations for the input seismic with zero-phase synthetic trace. The maximum correlation occurs at a 13° phase rotation of the seismic data, which is taken as the zero-phase correction.
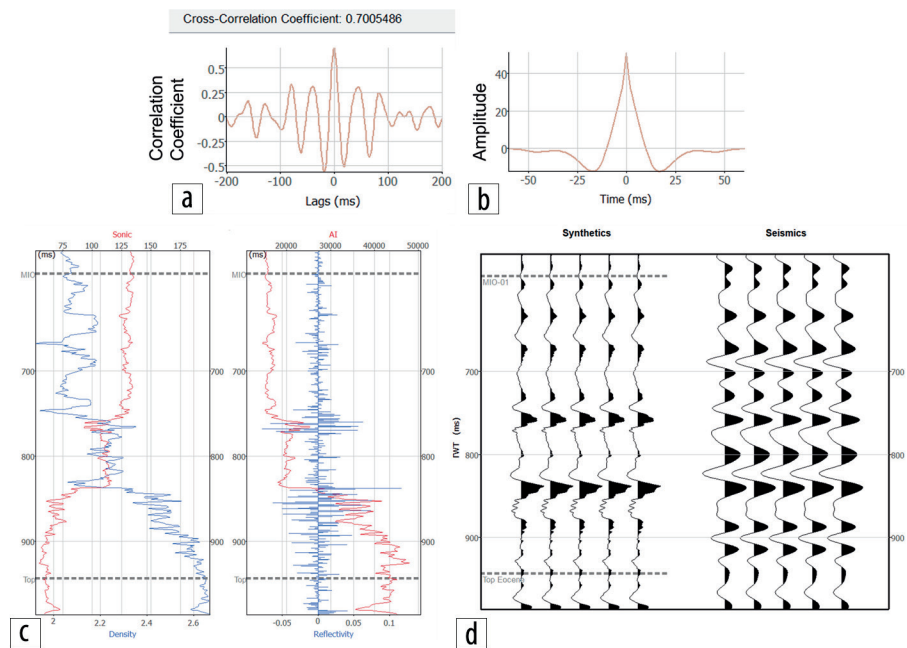

Figure 9. Well tie for the original seismic data after phase correction: (a) crosscorrelation time lags with max correlation; (b) extracted wavelet used for synthetic tie; (c) measured and derived logs used to compute synthetic; and (d) synthetic well tie to seismic.
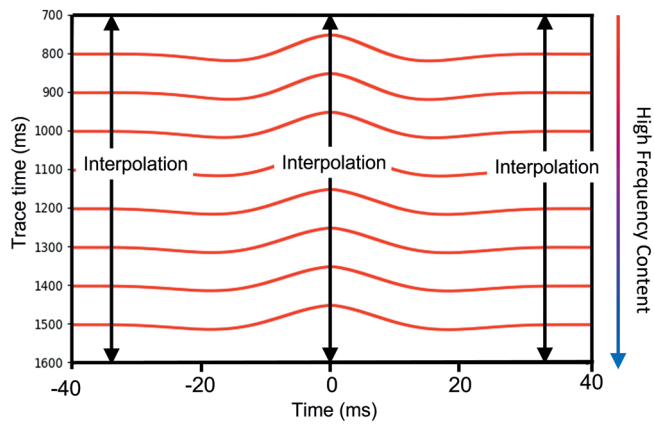
Figure 10. Time-variant wavelet extraction to compensate for attenuation. The wavelets are extracted in 500 ms windows at 100 ms node intervals and linearly interpolated in time. This method suppresses short-period energy related to local reflectivity, rock, and fluid properties.
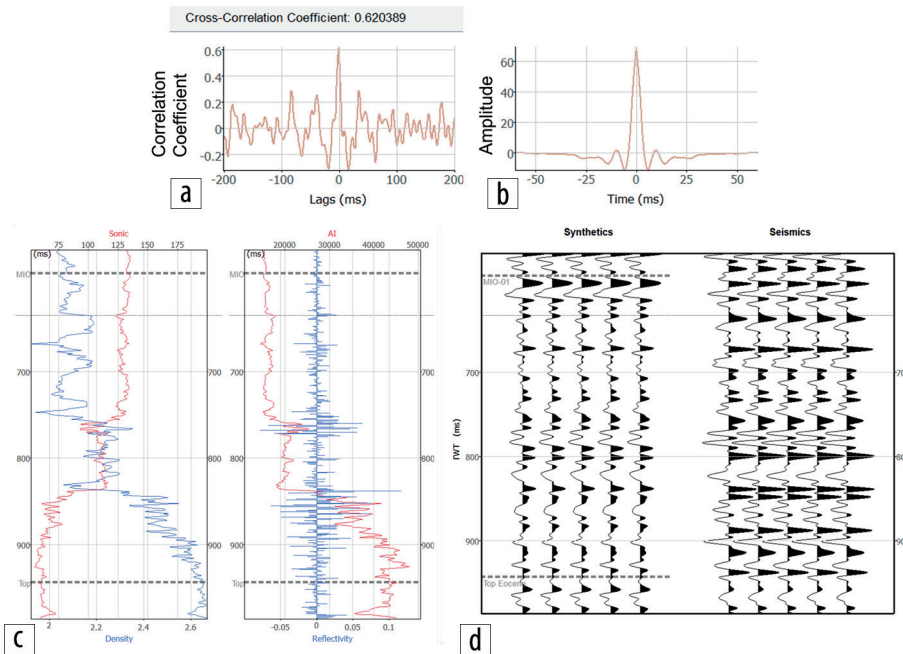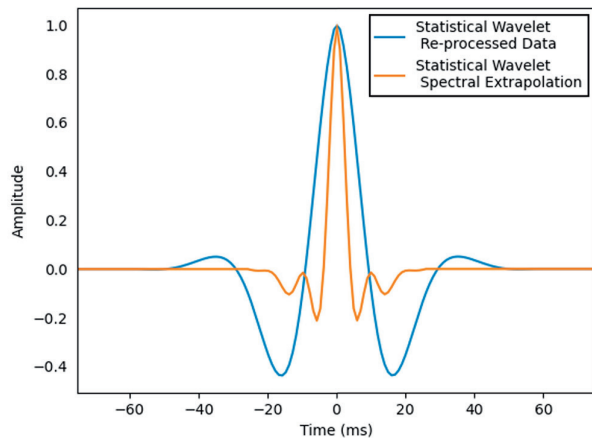
input seismic data and SE result are shown in Figure 12. Expansion in the frequency domain is equivalent to compression in the time domain. This is clearly illustrated in the plot, wherein the main lobe and sidelobe energies are far more concentrated around zero time. The spectra of the input seismic, band-passed, and SE data are shown in Figure 13. The input band-pass merely eliminates noise outside of the wavelet band. The SE data have approximately three times the frequency bandwidth of the input data, with a corresponding increase in resolution in the time domain.

Geologic observations. We compare the input and SE data around the well with log overplots (Figure 14). On the original band-limited seismic data, it is possible to identify key stratigraphic units and sequence boundaries. On the SE section, enhancements in stratigraphic detail are apparent throughout the section. The resolution and continuity of the events is observed not only within postrift sediments but also within Oligo-Miocene synrift and
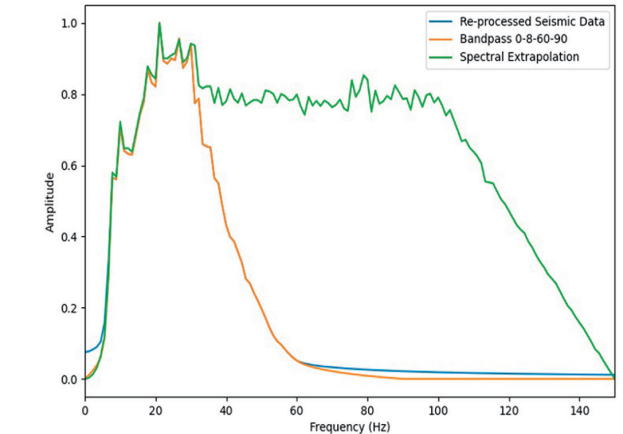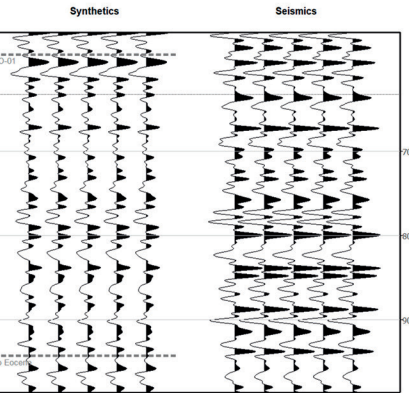

Figure 11. Well tie for SE data: (a) crosscorrelation time lags with max correlation; (b) extracted wavelet used for synthetic tie; (c) measured and derived logs used to compute synthetic; and (d) synthetic well tie to SE.

Figure 12. Statistical wavelets extracted for the input and SE data. The SE wavelet has significantly improved time compactness, indicative of a higher-resolution seismic image.

Figure 13. Bulk spectra for the seismic, band-passed, and SE data. The band-pass filter zeros noise outside of the wavelet spectrum in preparation for SE. SE approximately triples the frequency range of the data, with corresponding resolution enhancement in the time domain.

even prerift sections. Notably, we do not merely observe "thinning" of layers or convergence of top/base interfaces but also complex changes in thickness and morphology that are geologically plausible, consistent with the depositional history, and warrant further investigation. Thin layers observed in the SE result also correspond to those in the logs and synthetic.

Additional geologic features such as other pinch outs, unconformities, channels, and faults can also be mapped with the higher-resolution seismic. For example, the yellow box on Figure 14 shows the zoom limits of Figure 15 with a preliminary interpretation identifying the target pinch out using the SE high-resolution seismic result; this is not obvious when interpreting the original seismic data. Notice that the "truncation" surface apparent after application of the SE could be a small offset thrust fault. According to Sarewitz and Karig (1986), the Plio-Pleistocene tectonic activity produced some compressional features with a prominent eastward-dipping thrust fault mapped just to the east of the seismic line. The observed geometry of the "truncation" surface and age of the offset strata would be consistent with another small-scale thrust.

Enhancement of the subsurface image is a subject of further detailed interpretation, but it is obvious that application of SE led to improved stratigraphic and structural definition. This, in turn, allows better interpretation and understanding of petroleum system elements.

Conclusions

We have summarized the principles of SE and applied the technique to a legacy onshore 2D Philippines seismic data set, demonstrating that BE of seismic data is both feasible and geologically revealing. The process can be applied to full stack or angle

stack data, ideally with careful processing of amplitudes. While well logs are not required for the process, a good synthetic tie can be used to calibrate the phase and validate the input and SE data to generate higher confidence in the results. Refinements to the
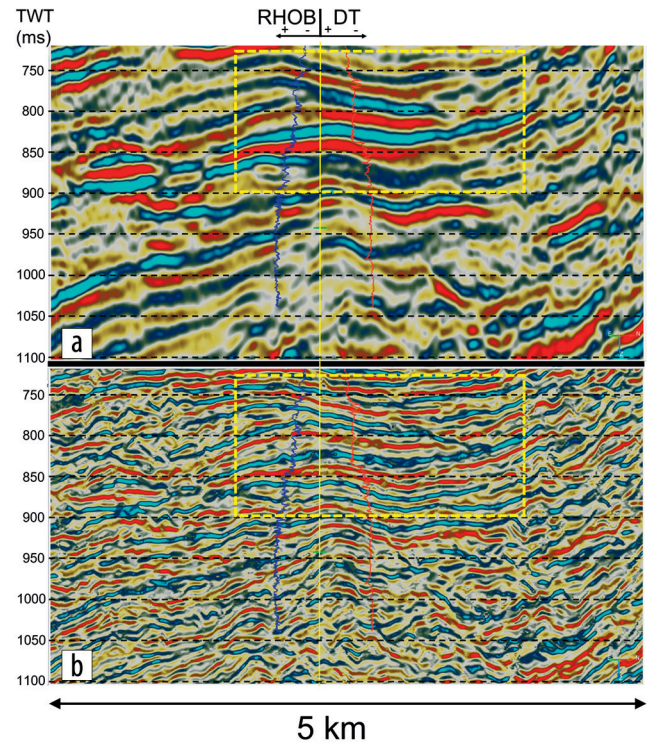

Figure 14. (a) Input seismic data and (b) SE with sonic and density logs (red and blue, respectively). Enhancements in stratigraphic and geomorphological detail are apparent throughout the section. The yellow box shows the zoom limits for Figure 15 interpretation.
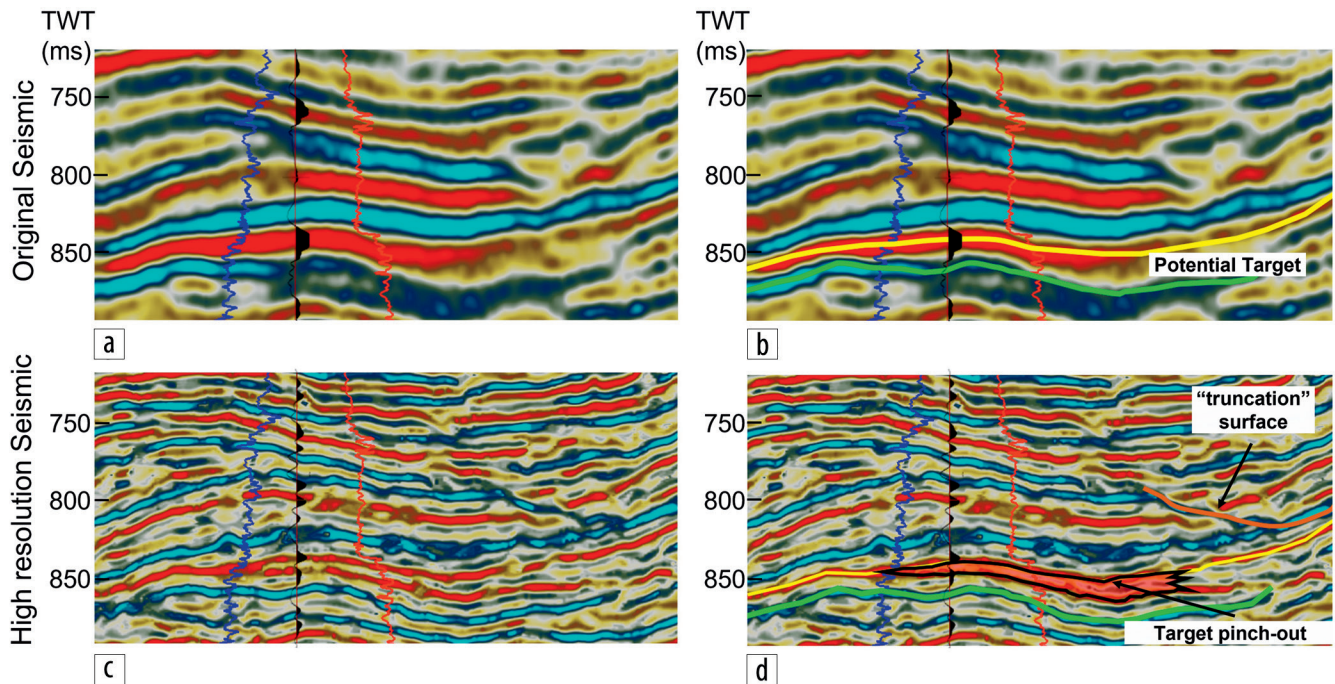

Figure 15. Zoomed-in section shows (a) original seismic data with logs and synthetic (black) and (b) with interpretation. Yellow and green lines show interpreted top and base of target, respectively. (c) The SE data with logs and synthetic (black) and (d) with interpretation. Target pinch out is well defined. Note the improvements in interpretation detail using the SE data.

input such as amplitude/phase Q compensation will simply propagate into the SE results. The resulting bandwidth is primarily limited by the input band, signal-to-noise ratio, and accuracy of the wavelet extraction — not the "tuning thickness" criterion. Based on sound physical principles with established mathematical definitions, the technique can be applied to a variety of seismic data types and integrated into quantitative interpretation workflows (i.e., seismic attributes, inversion, machine learning, etc.) for improved well placement, with relatively minimal cost outlay, in both exploration and production settings. **TLE**

Acknowledgments

Data and materials availability

Data associated with this research are confidential and cannot be released.

Corresponding author: charles@spectralgeosolutions.com

References

Aarts, R. M., E. Larsen, and O. Ouweltjes, 2003, A unified approach to low- and high-frequency bandwidth extension: Presented at the Audio Engineering Society 115th Convention, paper 5921.

Bird, P. R., N. A. Quinton, M. N. Beeson, and C. Bristow, 1993, Mindoro: A rifted microcontinent in collision with the Philippines volcanic arc; basin evolution and hydrocarbon potential: Journal of Southeast Asian Earth Sciences, **8**, no. 1–4, 449–468, https://doi.org/10.1016/0743-9547(93)90045-Q.

Brouwer, F., and A. Huck, 2011, An integrated workflow to optimize discontinuity attributes for the imaging of faults, *in* K. J. Marfurt, D. Gao, A. Barnes, S. Chopra, A. Corrao, B. Hart, H. James, J. Pacht, and N. C. Rosen, eds., Attributes: New views on seismic imaging — Their use in exploration and production: SEPM Society for Sedimentary Geology, https://doi.org/10.5724/gcs.11.31.0496.

Canadas, G., 2002, A mathematical framework for blind deconvolution inverse problems: 72nd Annual International Meeting, SEG, Expanded Abstracts, 2202–2205, https://doi.org/10.1190/1.1817146.

Cui, T., and G. F. Margrave, 2014, Seismic wavelet estimation: CREWES Research Report, **26**.

Friedlander, M. P., and M. A. Saunders, 2019, Active set methods for basis pursuit denoising, https://friedlander.io/files/pdf/bpprimal.pdf, accessed 12 December 2022.

Jones, H. J., and J. A. Morrison, 1954, Cross-correlation filtering: Geophysics, **19**, no. 4, 660–683, https://doi.org/10.1190/1.1438036.

Lazaratos, S., and C. Finn, 2004, Deterministic spectral balancing for high-fidelity AVO: 74th Annual International Meeting, SEG, Expanded Abstracts, 219–223, https://doi.org/10.1190/1.1851212.

Leiceaga, G. G., and C. I. Puryear, 2019, Spectral extrapolation and acoustic inversion for the characterization of an ultra-thin reservoir: 89th Annuual International Meeting, SEG, Expanded Abstracts, 3190–3194, https://doi.org/10.1190/segam2019-3209484.1.

Margrave, G. F., 1998, Theory of nonstationary linear filtering in the Fourier domain with application to time-variant filtering: Geophysics, **63**, no. 1, 244–259, https://doi.org/10.1190/1.1444318.

Partyka, G., 2005, Spectral decomposition and spectral inversion: SEG Distinguished Lecture series.

Portniaguine, O., and J. P. Castagna, 2005, Spectral inversion: Lessons from modeling and Boonesville case study: 75th Annual International Meeting, SEG, Expanded Abstracts, 1638–1641, https://doi.org/10.1190/1.2148009.

Puryear, C. I., and J. P. Castagna, 2008, Layer thickness determination and stratigraphic interpretation using spectral inversion: Theory and application: Geophysics, **73**, no. 2, R37–R48, https://doi.org/10.1190/1.2838274.

Puryear, C. I., R. Tharimela, and V. Egorov, 2021, Spectral extrapolation and random forest for high resolution prediction of subsurface properties: First International Meeting for Applied Geoscience & Energy, SEG/AAPG, Expanded Abstracts, 2119–2123, https://doi.org/10.1190/segam2021-3594792.1.

Rubino, J. G., and D. R. Velis, 2009, Thin-bed prestack spectral inversion: Geophysics, **74**, no. 4, R49–R57, https://doi.org/10.1190/1.3148002.

Sarewitz, D. R, and D. E., Karig, 1986, Geologic evolution of Western Mindoro Island and the Mindoro Suture Zone, Philippines: Journal of Southeast Asian Earth Sciences, **1**, no. 2, 117–141, https://doi.org/10.1016/0743-9547(86)90026-7.

Zhang, R., and J. Castagna, 2011, Seismic sparse-layer reflectivity inversion using basis pursuit decomposition: Geophysics, **76**, no. 6, R147–R158, https://doi.org/10.1190/geo2011-0103.1.